AIChE WILEY InterScience DISCOVER SOMETHING GREAT

SEPARATIONS

Modeling Nanofiltration with Nernst-Planck Approach and Polarization Layer

S. Déon, P. Dutournié, and P. Bourseau
Laboratoire d'Etudes Thermiques, Energétiques et Environnement, Université de Bretagne Sud, rue Saint-Maudé, BP 92116, 56 321 Lorient, France

DOI 10.1002/aic.11207
Published online June 13, 2007 in Wiley InterScience (www.interscience.wiley.com).

Selectivity prediction of charged solutions separation by nanofiltration membranes with a two-dimensional (2-D) model, combining transport through the membrane and polarization layer (PPTM) is presented. Pore transport is based on the Donnan Steric Pore Model (DSPM) with dielectric reassessment, and transport within the polarization layer is modeled from a steady-state mass balance, including turbulence influence on diffusion and velocity profiles, as well as wall influence on species diffusion very close to the wall. Specific experiments with glucose and concentrated NaCl solutions were carried out to determine membrane characteristics (average pore radius, charge density, dielectric constant of solution in the pore), and to adjust other model parameters. The model is then validated by comparing simulated rejections and experimental ones for other NaCl concentrations. With adjusted parameters, the model is able to predict local variations of rejection and permeation flux along the tubular membrane, as well as global observed rejections. © 2007 American Institute of Chemical Engineers *AIChE J,* 53: 1952–1969, 2007

Keywords: nanofiltration, transport phenomena, polarization layer, 2-D model, extended Nernst-Planck equation

Introduction

Nanofiltration (NF) is a recent pressure-driven membrane separation process, which has intermediate performances between reverse osmosis (RO) and ultrafiltration (UF) from both weight cut-off (100–1,000 Da) and transmembrane pressure (5–40 bars) points of view. Size of the NF membrane pores is approximately one nanometer, so they can be considered either as a nonporous skin, in which the transport is governed by the solution-diffusion mechanism, such as in RO separation, or as a porous media, such as UF membranes.

NF membranes allow small molecules to be separated according to size and charge exclusion effects of UF, and to solute-membrane interaction mechanisms of RO. These properties enable good selectivity between neutral solutes which are retained according to their size, monovalent ions, which are well transmitted and multivalent ions, which are mostly rejected. Moreover, this technology has the main advantage to require lower energy than RO, and to produce higher flux rates. Hence, this process is an innovative technology, which finds many applications in the fractionation or removal of specific solutes in industry, such as water softening, demineralization of biological solutions and effluent treatment. Furthermore, nanofiltration is a very competitive separation process which presents many advantages with respect to other processes because of its easy control, lower energy consumption, and environmental respect, that is, it does not require chemical addition.

Controlling the separation selectivity requires the understanding of physical phenomena occurring during the transport through the membrane. Many authors have described the various transfer mechanisms which manage the separation of charged or uncharged solutes according to three main

Correspondence concerning this article should be addressed to P. Dutournié at Patrick.dutournie@univ-ubs.fr.

approaches usually quoted in literature. The first approach was developed for uncharged solutes, such as sugar, and is based on the relation between driving forces and solute flux. The *hydrodynamic model* assumes that membrane is a porous media represented as a network of straight cylindrical pores uniformly dispersed in which solute transport is a combination of convection generate by solvent flux and diffusion caused by the concentration gradient in pores.[1] For charged solutes, the most frequently used is the *space-charged model* developed by Osterle et al.[2] and Dresner.[3] This model was used in the DSPM proposed by Bowen et al. in 1996, which is an improvement of the hydrodynamic's equation in which the transport is assumed to be also due to electrical potential gradient along pores.[4] This model, based on the *extended Nernst-Planck equation,*[5] assumed that concentration and potential are radially constant in the pore. This assumption is reasonable for nanofiltration membranes for which surface charge density is small and pores are sufficiently narrow. Within the second approach, transport of a solute is modeled by writing equilibrium between driving forces acting on the solute and friction forces with other components by means of *Maxwell-Stefan equation.*[6–8] This approach is suitable in particular for concentrated solutions. The last approach, which relies on *thermodynamics of irreversible process,* has been initiated by Kedem and Katchalsky,[9] and modified by Spiegler and Kedem.[10]

Even if mass transport through nanofiltration membrane is assumed to be well described, the prediction of separation selectivity between ions requires knowledge about solutes accumulation close to the wall. This concentration polarization has to be assessed either experimentally, by means of a global mass-transfer coefficient,[11,12] or by modeling the polarization layer. Polarization modeling can be carried out through the extended Nernst-Planck equation without friction terms, by assuming that the polarization layer is an ideal membrane with an infinite porosity.[13] In this approach, the global mass-transfer coefficient is either estimated from experiments by the velocity variation method,[14] or calculated with Sherwood correlations. The drawback of this 1-D method is that it does not take account of layer heterogeneity along the membrane. Thus, some authors have proposed a 2-D method by setting up a differential mass balance in the flow.[15] These authors assume that solutes accumulation is entirely contained in the viscous hydrodynamic sublayer.

In this article, a global 2-D model called "pores and polarization transport model" (PPTM), combining ions transport through the membrane and the polarization layer is presented. Membrane transport is described by the extended Nernst-Planck equation as proposed by Dresner.[3] Transport through the polarization layer is modeled by a differential mass balance in the flow as proposed by Bhattacharjee et al.,[15] but it is considered here that diffusion occurs not only into the viscous sublayer, but also in the buffer layer. This 2-D vision seems to be more suitable than the 1-D film theory, as it can describe the axial polarization layer heterogeneity along the membrane module.

This article begins with a physical description of the different physical phenomena occurring in the membrane, at the membrane/solution interface, and in the polarization layer. In the second part, the development of the 1-D membrane model, as well as the global 2-D model including polarization effects are described in detail. Thus, the experimental characterization of the membrane carried out by model parameters fitting from specific experiments is presented. After all, simulated rejection rates obtained with salts solutions (NaCl and $MgCl_2$) are determined for various operating conditions (tangential velocity, transmembrane pressure and bulk concentration), and are compared with experimental data.

Physical Description

This section is devoted toward describing physical phenomena occurring during separation of ionic solutions by nanofiltration membranes. Separation selectivity is mainly governed by the transport in the membrane, and the transfer through the membrane-solution interface by the way of equilibrium partitioning. However, selectivity is also influenced by transport through the polarization layer, which is caused by solutes accumulation near the wall due to permeation.

Transport phenomena

The model presented in this article is based on the Donnan-steric pore model, DSPM, proposed for the prediction of dye-salt diafiltration selectivity.[16] In this approach, membrane is considered as a porous medium composed of cylindrical single nanometer-sized pores uniformly dispersed. The transport modeling in the membrane is based on the extended Nernst-Planck equation,[5] which states that the flux of component *i, j_i*, is the sum of a flux, due to electrochemical potential gradient and convective flux, due to solute dragging by solvent flow

$$j_i(x) = -\frac{D_i}{RT} c_i(x) \frac{d\mu_i^*}{dx} + c_i(x) V \tag{1}$$

with x the step along the pore.

Concentrations within the pores are sufficiently small to assume that molecular diffusivity D_i, corresponds to diffusivity at infinite dilution $D_{i,\infty}$. This equation is usually modified by introducing hindered factors for convection $K_{i,c}$, and for diffusion $K_{i,d}$, accounting for the effect of finite pore size, as proposed by some authors.[17,18] The relations used to determined the coefficients $K_{i,c}$ and $K_{i,d}$[19] are presented in Table 1.

Electrochemical potential of the ith component is defined as

$$\mu_i^* = \mu_i^0 + RT \ln a_i + \overline{V}_i \left(p - p^0\right) + z_i F \psi \tag{2}$$

where μ_i^0, p^0, $\overline{V}_i$, and a_i are, respectively, the standard chemical potential, the reference pressure, the partial molar volume, and activity of ion i. ψ is the electrical potential within the pore, due to charge accumulation close to the pore wall.[4]

If solutions are not assumed to be infinitely diluted then activity coefficients are proportional to concentration through activity coefficient γ_i ($a_i = \gamma_i C_i$). Expression of ionic flux of component i becomes[20]

$$j_i(x) = -c_i K_{i,d} D_{i,\infty} \frac{d[\ln \gamma_i]}{dx} - K_{i,d} D_{i,\infty} \frac{dc_i}{dx} - \frac{K_{i,d} D_{i,\infty}}{RT} c_i \overline{V}_i \frac{dp}{dx} - \frac{z_i c_i K_{i,d} D_{i,\infty}}{RT} F \frac{d\psi}{dx} + K_{i,c} c_i V \tag{3a}$$

Table 1. Constant Model Parameters

Parameters	Values	References
Ionic diffusivity at infinite dilution (10^{-9} $m^2.s^{-1}$)	$D_{\infty,Na^+} = 1.334$ / $D_{\infty,Mg^{2+}} = 0.706$ / $D_{\infty,Cl^-} = 2.031$	48
Stokes radius (10^{-10} m)	$r_{Na^+} = 1.84$ / $r_{Mg^{2+}} = 3.48$ / $r_{Cl^-} = 1.21$	38
Membrane radius (m)	R = 6.35 10^{-3}	–
Temperature (K)	T = 298	–
Hindered factor for convection	$K_{i,c} = (2 - \phi)\cdot(1 + 0{,}054\ \lambda - 0{,}988\ \lambda^2 - 0{,}441\ \lambda^3)$	60
Hindered factor for diffusion	$K_{i,d} = (1 - 2{,}30\ \lambda + 1{,}154\ \lambda^2 + 0{,}224\ \lambda^3)$	60
Dielectric constant of water at 25°C	$\varepsilon_b = 78.4$	48

It is usually assumed that concentrations and their variations along the pore are sufficiently small to allow one to neglect the gradient of $ln\gamma_i$. Some authors also assume that partial molar volumes of solutes are sufficiently small to neglect the pressure gradient contribution in the electrochemical gradient. These assumptions were validated by a sensitivity study with our model, and ionic flux is expressed, as it was done by most of the authors,[21–24] by the extended Nernst-Planck Eq. 3b in the simplified form

$$j_i = -D_{i,p}\frac{dc_i}{dx} - \frac{z_i c_i D_{i,p}}{RT}F\frac{d\psi}{dx} + K_{i,c}c_i V \tag{3b}$$

where $D_{i,p}$ is the diffusion coefficient of the i-th component within the pores ($D_{i,p} = K_{i,d}D_{i,\infty}$), and the solvent velocity within the pore V is related to the pressure gradient through the pore using the Hagen-Poiseuille expression

$$V = \frac{{r_p}^2\Delta P_e}{8\eta\Delta x} = \frac{{r_p}^2[\Delta P - \Delta\pi]}{8\eta\Delta x} \tag{4}$$

where Δx is the membrane thickness.

Equilibrium partitioning

A - Neutral Molecules. For neutral solutes, equilibrium partitioning is solely governed by steric effects. Ferry[25,26] introduced a steric partitioning coefficient ϕ_i, linking the concentrations of component i on both sides of the interface. This coefficient ϕ_i is expressed on a geometric basis, through λ_i, the ratio of the Stokes radius of specie i, r_i, to pore radius r_p[27]

$$\phi_i = \frac{c_i}{C_i} = \left(1 - \frac{r_i}{r_p}\right)^2 = (1 - \lambda_i)^2 \tag{5}$$

where c_i and C_i are, respectively, the concentrations at the pore and solution sides of the interface ($c_i = c_i(0)$, and $C_i = C_{i,w}$ at the pore inlet, $c_i = c_i(\Delta x)$, and $C_i = C_{i,p}$ at the pore outlet). The various radii of ions are given in Table 1.

B - Charged Molecules. Equilibrium partitioning of ionic molecules is the most fundamental phenomenon acting on selectivity. First based on Donnan equilibrium theory, it has been improved by several authors by introducing new phenomena, which was not taken into account with Donnan equilibrium, such as steric or dielectric effects.

1. Donnan equilibrium states the equality of electrochemical potential of solutions on both sides of the membrane interface

$$\mu_i^0 + RT\ln(a_{i,s}) + z_i F\psi_s = \mu_i^0 + RT\ln(a_{i,m}) + z_i F\psi_m \tag{6}$$

ψ_s and ψ_m are, respectively, the electrical potentials of the solutions on the flow and pores sides of the membrane interface.

So, the activities ratio on both sides can be expressed as

$$\frac{a_{i,m}}{a_{i,s}} = \exp\left(-\frac{z_i F}{RT}\Delta\psi_D\right) \tag{7}$$

where $\Delta\psi_D = \psi_m - \psi_s$ called the Donnan potential, is the same for each ion in the solution.[28]

Combining Donnan equilibrium and steric partitioning coefficient ϕ_i expressed in the previous paragraph leads to the most common partitioning expression[23,29,30]

$$\frac{\gamma_{i,m}c_i}{\gamma_{i,s}C_i} = \phi_i\exp\left(\frac{-z_i F}{R.T}\Delta\psi_D\right) \tag{8}$$

where $\gamma_{i,s}$ and $\gamma_{i,m}$ are the activity coefficients of the i-th ion on both sides of the interface, respectively, in the solution and within the pore. The activity coefficients of the ions in the membrane $\gamma_{i,m}$, are estimated by the well-known Debye-Hückel equation

$$\log\gamma_i = \left(\frac{-{z_i}^2 A_2\sqrt{I}}{1 + A_1 r_i\sqrt{I}}\right) \tag{9}$$

where r_i is the ionic radius of i-th ion in angström, and I is the ionic strength in mol/L. Coefficients A_1 and A_2 are taken, respectively, equal to 0.329 and 0.509 in the case of water solution at 25°C.[31] Within the polarization layer, in the case of pure salt solutions, an average activity coefficient, suitable even for high-concentrations, is calculated by an extended Debye-Huckel equation[32]

$$\ln\gamma_{+-} = \left(\frac{z_+ z_- A_2\sqrt{I}}{1 + A_1 r_i\sqrt{I}}\right) + A_3 C_{salt} \tag{10}$$

where the value of the coefficient A_2 is 1.1779, and the values of A_3 are given by Newman et al.[32] for various reference values of $A_1 r_i$ depending on the salt type. For example, in the case of a NaCl solution, $A_1 r_i$ is taken equal to 1 $(kg/mol)^{0.5}$, and the value of $A3$ given by Newman et al. is 0.15. The activity coefficients of the ions are then calculated by assuming that $\gamma_+ \cong \gamma_- \cong \gamma_{+-}$, which is tolerable

because the error between γ_+ or γ_- and γ_{+-} is always lower than 2%.

Influence of the activity coefficients on rejection is usually neglected, but simulations have shown that it is quite fundamental to describe physical phenomena occurring at the membrane interface, that is, it can modify the rejection up to 10 percent.

2. The last mechanism influencing the selectivity of a membrane separation of charged solutes is dielectric phenomenon, generated by water dipole moment and ions charges. Both electric (Donnan equilibrium) and dielectric exclusion modifies the rejection of charged species, but it should be noticed that they act in a different way. Electric exclusion is favorable or unfavorable to ions transfer through the membrane/solution interface according to their charge sign. On the contrary, dielectric exclusion always lessens the transfer whatever the ions sign is.

Physico-chemical mechanisms due to these dielectric differences can be classified into three types:[33]

- Dispersion interactions occurring between ions within pores and membrane materials, which are neglected by all authors.
- Dielectric exclusion resulting from interactions between ions and the so-called "image charges" generated at interfaces separating media with different dielectric properties. In the membrane pore, the dielectric constant of the electrolyte ε_p is higher than that of the membrane material ε_m (supposed to be that of polyamide material in our case, that is, $\varepsilon_m = 3$). "Image forces" have been introduced by Dukhin et al.[33] for dense reverse osmosis membranes, and has been discussed in detail by Yaroshchuk[34,35] for porous nanofiltration membrane. Yaroshchuk has described this mechanism for slit-like capillaries by the following equation (a more complicated relation is provided for cylindrical pores, but Szymczyk and Fievet found that the best description of an AFC 30 membrane is obtained by modeling the membrane as a bundle of slit-like pores[29])

$$\Delta W_{i,im} = -\frac{r_B}{r_p}\ln\left(1-\frac{\varepsilon_p-\varepsilon_m}{\varepsilon_p+\varepsilon_m}\exp(-2r_p\kappa_p)\right)+r_B(\kappa_s-\kappa_p) \tag{11}$$

where κ_s and κ_p are the inverse of the Debye lengths within, respectively, the solution and the pores, and r_b is the Bjerrum radius

$$r_B = \frac{(z_i e)^2}{8\pi\varepsilon_0\varepsilon_p k_B T} \quad \text{and} \quad \kappa = F\sqrt{\frac{2I}{\varepsilon_0\varepsilon RT}} \tag{12}$$

The second term of Eq. 11 appears because concentration within the pores is really different from that of the bulk solution. This term corresponds to an activity coefficients variation on both sides of the interface. In our case, this correction was already included in the model through the ratio of activity coefficients in the interface partitioning (cf. Eq. 8).

- The last mechanism imputed to dielectric effects is the appearance of an energy barrier to solvation caused by confinement of water molecules within pores. Indeed, Israelachvili[36] showed in 1991, from electrochemical studies of colloidal systems, the presence of a layer of oriented water molecules with a different dielectric constant at the colloid-solvent interface. In the same way, oriented water molecules at the pores wall tend to reduce the solution dielectric constant within the pore. The dielectric effect due to the solvation energy barrier in the equilibrium partitioning can be described by the Born model of solvation energy barrier[37]

$$\Delta W_{i,born} = \frac{z_i^2 e^2}{8\pi\varepsilon_0 k_B T r_i}\left(\frac{1}{\varepsilon_p}-\frac{1}{\varepsilon_b}\right) \tag{13}$$

where ε_p and ε_b are, respectively, the dielectric constants of the solution within the pores and bulk solution, and ε_0 is the permittivity of free space.

The most general equation of equilibrium partitioning which takes all of the effects into account is then

$$\frac{c_i}{C_i} = \phi_i{}' \exp\left(\frac{-z_i F}{RT}\Delta\psi_D\right) \tag{14}$$

The Donnan potential $\Delta\psi_D$ is the same for each ion, so equilibrium partitioning between two ions i and j can be written from Eq. 14

$$\left(\frac{c_i}{\phi_i{}' C_i}\right)^{\frac{1}{z_i}} = \left(\frac{c_j}{\phi_j{}' C_j}\right)^{\frac{1}{z_j}} \tag{15}$$

where ϕ' is a coefficient grouping the influences of the activity coefficients ratio, and the steric and dielectric effects

$$\phi_i{}' = \frac{\gamma_{i,s}}{\gamma_{i,m}}\phi_i \exp\left(-\Delta W_{i,born}\right)\exp\left(-\Delta W_{i,im}\right) \tag{16}$$

It is worth mentioning that recent works have shown good agreement between experimental and simulated rejections by taking the dielectric effect into account, including either Born energy barrier only,[30,38] or only the "image forces".[39] All these authors obtained reasonable results because the differences are located in the type and the values of the adjustable parameters. Introducing all of the physical phenomena as it was done by Szymczyk et al.[29] probably allows one to have physical values closer to the reality, but one dielectric phenomenon seems to be sufficient to describe the dielectric exclusion, even if the other could not be neglected. For this reason, the dielectric effect due to the "image forces" was not included in this study, and only Born effect is considered, as it leads to more realistic values of dielectric constant within the pores ε_p (cf. § "Results and Discussion").

Concentration polarization layer

A - Observed and Real Rejection Rates. Membranes performances are usually defined by permeation flux and the rejection rate (or rejection) of the various solutes. The observed rejection of solute i is defined from permeate and bulk concentrations as

$$R_{i,obs} = 1 - \frac{C_{i,p}}{C_{i,r}} \tag{17}$$

The interest of this parameter is that it can be easily calculated from experimental measurements, but it has the draw-

back to be not characteristic of membrane selectivity. Indeed, solutes accumulation at the membrane surface due to solvent permeation leads to a concentration of solute i at the membrane wall $C_{i,w}$ greater than the bulk concentration $C_{i,r}$. So, the real (or intrinsic) membrane rejection $R_{i,m}$ is greater than the observed one. $R_{i,m}$ is defined as

$$R_{i,m} = 1 - \frac{C_{i,p}}{C_{i,w}} \tag{18}$$

where $C_{i,w}$ is the concentration of the i-th solute (or ion) very close to the membrane wall. This real rejection is an intrinsic characteristic of the membrane-solution couple, as it is independent of module geometry, and of U_t (and more generally of hydrodynamic conditions).

B - 2-D Model Theory. In this section, we present a global 2-D model PPTM combining a 2-D modeling of polarization layer, and the 1-D membrane transport (interfaces partitioning and transport through the membrane).

Modeling the polarization layer establishment near the membrane wall required some assumptions:

- Flow is assumed to be turbulent and steady.
- Turbulence is described by the pseudo-laminar model for which velocity and concentration are time-smoothed, and turbulent mass transfer is assumed to follow a Fick-like diffusion law with eddy diffusivity.
- Axial diffusion along the membrane is negligible compared with convection flux in the same direction.
- Permeation flux is low-enough compared with the feed flow rate to neglect the permeation influence on the velocity profile.
- The membrane wall is assumed to be flat, neglecting curvature influence, and so the equations are written in Cartesian coordinates (y is the transverse distance from membrane wall $R - r$, and z is the axial coordinates).

The concentration polarization development for binary ionic mixture can be described by a steady-state differential mass balance,[40,41] where diffusion is defined by Fick's law

$$u(y)\frac{\partial C_i(y,z)}{\partial z} + v(y,z)\frac{\partial C_i(y,z)}{\partial y} = D_i(y)\frac{\partial^2 C_i(y,z)}{\partial y^2} \tag{19}$$

where $u(y)$ is the axial velocity in the z direction, and v the radial velocity due to permeation flux. C_i is the concentration of i-th ion, and D_i is its effective diffusivity, defined from the pseudo-laminar model as the sum of molecular and turbulent diffusivities ($D_i(y) = D_{i,m} + D_{i,t}(y)$). In this study, only single salt solutions are considered, and ions are assumed to diffuse at the same velocity (as a single substance) within the polarization layer due to electroneutrality. So, the cation and the anion are considered having the same molecular diffusivity, that is, the salt diffusivity defined as

$$D_{salt} = \frac{(z_+ + |z_-|)D_+D_-}{z_+D_+ + |z_-|D_-} \tag{20}$$

where D_+ and D_- are the ions diffusivities. In this study, molecular diffusivities of ions $D_{i,m}$ are taken at infinite dilution, and their values are given in Table 1. Indeed, a sensibility study has shown that the salt concentration influence on molecular diffusivity within the polarization layer could be neglected. The determination of the turbulent diffusivity is described in the next paragraph.

At the membrane interface, axial velocity equals to zero, and the mass balance becomes

$$\forall z \geq 0 \qquad J_v(C_{i,w} - C_{i,p}) = -D_{salt,w}\left(\frac{\partial C_i}{\partial y}\right) \tag{21}$$

where $D_{i,w}$ is the diffusion coefficient of the i-th component at the wall. This coefficient is initially approximated by the molecular diffusivity of the corresponding ions (or salts for pure salt solutions), but we will examine afterwards the influence of suction and roughness on this wall diffusivity.

Influence of activity coefficients variation on polarization is supposed to be negligible, and the molecular-diffusion coefficient is assumed to be constant within the polarization layer.

The boundary conditions are defined, respectively, at the membrane channel entrance and bulk solution by

$$z = 0,\ \forall y \geq 0 \qquad C_i(0,y) = C_{i,r} \tag{22a}$$

$$\forall z \geq 0,\ \ y \geq \delta(z) \qquad C_i(z,y) = C_{i,r} \tag{22b}$$

where $C_{i,r}$ is the bulk concentration of the i-th component in the retentate, and $\delta(z)$ the thickness of the polarization layer at the abscissa z.

Some authors have efficiently initiated the modeling of the polarization layer,[15,41,42] by assuming that solutes accumulation is wholly contained in the laminar hydrodynamic sublayer in which velocity is assumed to be linear. Our global 2-D model is an improvement of these models, considering the fact that solutes accumulation also occurs in the other hydrodynamic layers for which velocities and diffusion profiles have to be determined.

C - Velocities and Diffusion Profiles. Figure 1 presents the velocity profiles retained to model the turbulent flow within the membrane tube. The three different zones are determined by using the classical equations of hydrodynamics for turbulent flow in cylindrical pipe.[43,44]

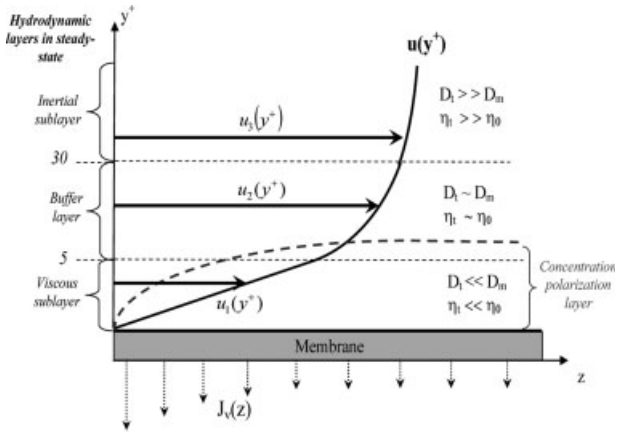

Figure 1. Velocity profile in hydrodynamic layers.

The different hydrodynamic layers are defined in terms of normalized wall distance, $y^+ = \frac{\rho y u^*}{\eta}$, where u^* is the friction velocity defined for smooth pipes from Blasius formula by

$$u^* = \sqrt{\frac{\tau}{\rho}} = \sqrt{\frac{0.5 \times U_t^2 \times 0.0791}{\mathrm{Re}^{0,25}}} \tag{23}$$

where τ is the wall shear stress.

The velocity profiles in the various hydrodynamic layers are defined by

in the viscous sublayer ($y^+ \leq 5$)

$$u_1(y^+) = u^* y^+ \left[1 - \frac{1}{4}\left(\frac{y^+}{14.5}\right)^3\right] \tag{24}$$

in the buffer layer ($5 \leq y^+ \leq 30$)

$$u_2(y^+) = u^*[5\ln(y^+ + 0.205) - 3.27] \tag{25}$$

in the inertial sublayer ($y^+ \geq 30$)

$$u_3(y^+) = u^*[2.5\ln(y^+) + 5.5] \tag{26}$$

Velocity profile in the main turbulent stream is not considered in this model, because it is well-known that polarization layer is fully developed in the hydrodynamic sublayers.

Simulations carried out with the fluid mechanic software Fluent showed that wall suction has no effect on axial velocity profile because radial flux is negligible compared to cross-flow rate. Moreover, hydrodynamic modeling based on the 2-D resolution of Navier-Stokes equations showed that the radial velocity decreases slightly in the hydrodynamic layers, but this variation can be neglected. So $v(z,y)$ is supposed to be constant along the y-axis ,and equals to the permeation velocity $J_v(z)$.

In the same way that velocity profile and turbulent-diffusion coefficients vary in the different hydrodynamic layer. It is usually assumed that eddy diffusivity D_t, and eddy-kinematic viscosity v_t, are of the same order of magnitude, based on the idea that momentum and mass transfers are similar. This approximation is totally suitable in the core where the flow is entirely turbulent. However, in the hydrodynamic sublayers, relation between viscosity and diffusion are not known, especially in the case of liquids, so it was chosen to link eddy diffusivity and viscosity with molecular diffusivity and bulk viscosity via Eq. 27. This approach is coherent with the continuity of diffusion between the various hydrodynamic sublayers

$$\frac{D_t}{D_m} = \frac{v_t}{v} \tag{27}$$

Thus, the eddy-diffusivity profile is determined from eddy viscosity v_t obtained from Prandtl's mixing length l[43,44]

$$v_t(y) = l^2\left|\frac{\partial u}{\partial y}\right| = (Kya)^2\left|\frac{\partial u}{\partial y}\right| \tag{28a}$$

where K is the Karman constant ($K = 0.4$), and is defined from the Van Driest model by

$$a = 1 - \exp\left(\frac{-y^+}{25}\right) \tag{28b}$$

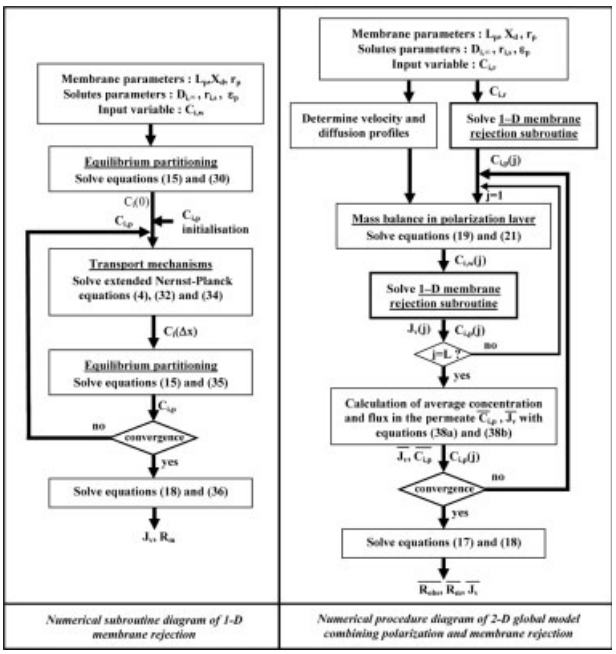

Figure 2. Numerical procedure diagram.

Model Development

The model presented in this article is based on the physical phenomena, and the associated assumptions described in the previous paragraph. In this model, some phenomena were not taken into account to describe the membrane transport, even if their influence on rejection cannot be neglected. Indeed, this article deals mainly with the description of the polarization modeling so some assumptions were made. For this reason, the electroviscous effect[13] on the salt permeability was not introduced in the model, and the permeability used to calculate the permeation flux is assumed to be that of water. The "image charges" term was also not included in the equilibrium partitioning, because Born solvation effect seems to be sufficient to describe the dielectric exclusion even if the influence of "image charges" is not negligible.

The resolution procedure of the model is presented on Figure 2. The prediction model of observed rejections of component i is developed in two parts. The first part describes the 1-D transport of ion i through the membrane, and the second one is a 2-D model of the polarization layer. The calculation is carried out by solving the latter iteratively, including the former as a subroutine.

Membrane rejection model (1-D)

1. First of all, concentration at pore entry ($x = 0$) for a given ion 1, $c_1(0)$ is calculated with an iterative bisection method from membrane wall concentration $C_{i,w}$ through equilibrium Eq. 16, combined with electroneutrality in the pore for n ions

$$\sum_{i=1}^{n} z_i c_i + X_d = 0 \tag{29}$$

where X_d is the membrane charge density, which can be assessed by the model or estimated with experimental char-

acterization process, such as streaming or membrane potentials.[45–47]

Thus, combining Eqs. 16 and 29 leads to

$$z_1 c_1(0) + \sum_{j=2}^{n} \left[z_j \phi'_j C_{j,w} \left(\frac{c_1(0)}{\phi'_1 C_{1,w}} \right)^{z_j/z_1} \right] + X_d = 0 \qquad (30)$$

The wall concentration $C_{1,w}$ is calculated either by the polarization model for 2-D model, or it is taken equals to bulk concentration in the case of 1-D membrane rejection model.

Knowing $c_1(0)$, the pore entrance concentrations $c_i(0)$ of other ions are calculated from Eq. 16.

2. Solving membrane transport equations requires an additional equation, namely the mass conservation of ion i within the pores. Under the steady-state hypothesis, the flux of component i is constant along the pore and, can, thus, be evaluated at the pore output knowing V with Eq. 4

$$j_i(x) = j_i = VC_{i,p} \qquad (31)$$

Thus, concentration profiles along the pore are determined by rearranging the extended Nernst-Planck equation (Eq. 3b), including Eq 31, the value of the permeate concentration $C_{i,p}$, being that calculated at the previous global iteration (initialized at zero for the first iteration)

$$\frac{dc_i}{dx} = \frac{V}{D_{i,p}} \left(K_{i,c} c_i - C_{i,p} \right) - \frac{z_i c_i}{RT} F \frac{d\psi}{dx} \qquad (32)$$

Membrane charge density is assumed to be constant along the pore, so differentiation of Eq. 29 gives

$$\sum_{i=1}^{n} z_i \frac{dc_i}{dx} = 0 \qquad (33)$$

Multiplication of Eq. 32 by z_i, summation over all ions and introduction in the previous Eq. 33, gives the potential gradient (which is the same for all ions)

$$\frac{d\psi}{dx} = \frac{\sum_{i=1}^{n} \frac{z_i V}{D_{i,p}} \left(K_{i,c} c_i - C_{i,p} \right)}{\frac{F}{RT} \sum_{i=1}^{n} z_i^2 c_i} \qquad (34)$$

Concentration evolution along the pore $\frac{dc_i}{dx}$, is calculated by the Euler method for each component I, with Eqs. 32 and 34 with the initial boundary condition $c_i(0)$, obtained with equilibrium partitioning at the pore entrance.

3. Equilibrium partitioning, is, thus, used to calculate permeate concentration $C_{i,p}$, in the same way that inlet pore concentration from the pore outlet concentration $c_i(\Delta x)$. The equilibrium partitioning is obtained by introducing Eq. 15 in the electroneutrality equation within the permeate solution

$$z_1 c_{1,p} + \sum_{j=2}^{n} \left[\frac{z_j C_j(\Delta x)}{\phi'_j} \left(\frac{c_1(\Delta x)}{\phi'_1 C_{1,p}} \right)^{-z_j/z_1} \right] = 0 \qquad (35)$$

This procedure is started again at step 2, with the new values of permeate concentrations $C_{i,p}$, and reiterated until solution convergence, that is, until permeate concentration does not vary from an iteration to another. Permeation flux J_v is calculated by

$$J_v = \frac{L_p}{\eta} \left(\Delta P - \Delta \pi \right) \qquad (36)$$

where the membrane water permeability L_p is calculated from pure water experiments, and the osmotic pressure difference $\Delta\pi$ across the membrane is calculated using the Van't Hoff relation

$$\Delta \pi = RT \sum_{i=1}^{n} (C_{i,w} - C_{i,p}) \qquad (37)$$

The viscosity was corrected in terms of salt concentration from Handbook data.[48]

Global 2-D Pore and polarization transport model (PPTM)

The first step of the global model resolution procedure consists in initializing permeate concentrations and flux of all the components, with the 1-D rejection model using the bulk concentration $C_{i,r}$ as the wall concentration $C_{i,w}$.

When $C_{i,w}$ is initialized, the equations system describing physical phenomena in the flow (Eqs. 19 to 28) is expressed in a matrix form, and solved with a Gaussian elimination method.[49] The results are the concentrations evolution of ionic species in the layer $C_i(y^+)$ at a given z-abscissa, and the wall concentrations $C_{i,w}$ are used to calculate permeate concentrations with 1-D membrane rejection model.

This procedure is carried out all along the membrane (for $z = 0$ to L), using the concentration profiles $C_i(y^+)$ calculated at the previous z-step, and the permeate concentrations $C_{i,p}$ calculated at previous global loop. Average concentration $\overline{C_{i,p}}$, and permeation flux at the permeate outlet are calculated for each loop, by

$$\overline{C_{i,p}} = \frac{\sum_{j}^{m} J_v(z)\, C_{i,p}(z)}{\sum_{j}^{m} J_v(z)} \qquad (38a)$$

and

$$\overline{J_v} = \frac{\sum_{j}^{m} J_v(z)}{L} \qquad (38b)$$

One important point of this model is that permeate concentration is calculated locally at each z-value along the membrane, that is, it is assumed that there is no axial transport in the microporous media. There is, thus, no mixing at the pore outlet, and $C_{i,p}(z)$ at a given z-value is independent of its neighbors. The average concentration at the permeate outlet $\overline{C_{i,p}}$ is, thus, calculated by Eq. 38a.

Convergence is obtained when $\overline{C_{i,p}}$ does not vary from an iteration to another.

Experimental

Setup

The experimental equipment depicted in Figure 3 is a semi-industrial pilot-plant (T.I.A., Bollène, France), which

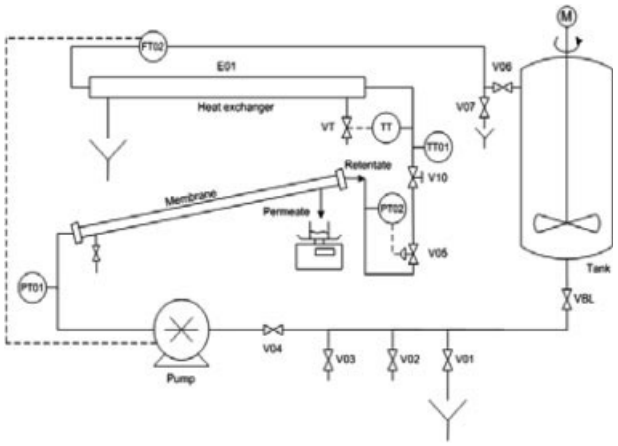

Figure 3. Experimental setup.

can be operated in tubular or spiral-wound configuration. For this study, an AFC40 tubular polyamide film membrane (d = 12.7 mm, L = 1.22 m) supplied by PCI Membrane Systems Ltd (Basingstoke, UK) was used. A volumetric triplex plunger pump supplied cross-flow rate from 500 l/h to 2,000 l/h, with pressure from 4 to 25 bars. Flow is controlled by an electromagnetic flowmeter. Pressure is measured by two sensors upstream and downstream of the membrane, and is regulated by an electropneumatic valve. Temperature is maintained constant at 25°C (± 0.5°C) through circulation in a countercurrent heat exchanger cooled by a frigorific unit. Concentrations are kept constant by recycling permeate into the feeding tank except during measurements for permeate flow rate calculation and sampling for concentration analyses.

Solutions

The AFC40 membrane average pore radius was assessed from experiments with neutral molecule (glucose).

To study the ionic selectivity of the membrane, various experiments were carried out with mineral single salts in solution in the range of [0, 0.2 M] for NaCl solutions, and [0, 0.1 M] for $MgCl_2$ solutions. Other experiments have been done at greater concentrations in order to estimate the dielectric constant of the solvent in the pore (0.4 M for NaCl solutions and 0.2 M for $MgCl_2$ solutions).

Water fluxes measurements, cleaning and salt solutions preparation were performed using demineralized water with a residual conductivity lower than 0.1 μS/cm.

Analyses

Ions concentrations in permeate and retentate were analyzed by an ionic chromatography apparatus (ICS 1000, Dionex, Voisins le Bretonneux, France) equipped with a conductivity detector for the measurements of ion concentrations. Single salt solutions were also analyzed with a double electrode probes conductimeter. Concentrations of glucose solutions were determined with an enzymatic colorimetric method using a GOD-PAP kit coupled with a UV/visible spectrometer.

Protocols

The membrane was first washed by basic-acid-basic cleaning sequence. Basic cleaning is performed with an Ecolab Ultrasil 53 solution, 5 g/L, 40°C, and an Ultrasil 75 solution, 3 ml/L, at room-temperature, is used for acid cleaning.

Before each experiment, pilot is cleaned and filled with demineralized water. Water flux is then measured for various pressure differences to check that hydrodynamic membrane characteristics do not change between experiments. Membrane permeability L_p is also calculated from water flux evolution with applied pressure difference for the membrane 1-D model.

Then, feed tank is emptied and filled with the salt solution, which is homogenized by circulation with high-flow velocity for 30 min. Then the pilot is run during one night at $Q = 1m^3/h$ $\Delta P = bar$, and to reach ionic adsorption equilibrium into the membrane pores.

After these preliminary steps, observed rejections are determined for different pressures and velocities. For each experimental point, the permeate flux is calculated by measuring the permeation flow rate, and both permeate and retentate are sampled for analyzes. Observed rejections are then calculated from Eq. 17, and plotted in terms of permeate flux for each velocity. From these experimental curves, real rejections are determined with the velocity variation method (see § Results and Discussion).

Preliminary experiments have proved that chemical cleaning of the membrane strongly affects the membrane characteristics, mainly its permeability, and also probably the membrane charge density. So, cleaning frequency has been limited, as much as possible by regularly operating the plant with pure water during the periods where no experiment was done. Nevertheless, a chemical cleaning has been performed between experiments with NaCl and $MgCl_2$ solutions because a decrease in water flux had been noted.

Results and Discussion

This section deals first with the model parameters determination, and second with the presentation of simulated results of salt rejection. These results are compared with those obtained experimentally to determine the validity of the presented model.

The model parameters can be classified in two categories: the membrane parameters (L_p, r_p, ε_p, and X_d), and the polarization parameter (α). The membrane parameters are assessed with the 1-D model, which describes the transport through the membrane and the equilibrium partitioning at the interfaces. The polarization parameter is calculated with the 2-D PPTM combining transport in the polarization layer and through the membrane.

1-Membrane characterization

The model presented in this study requires the determination of four parameters to describe the transport through the membrane: the membrane permeability L_p, the average pore radius r_p, the dielectric constant within the pore ε_p, and finally the membrane charge density X_d. The last one varies with ionic species and concentration, and has to be deter-

mined for each concentration to obtain a correlation between ion concentration within the pore and the membrane charge density. The three other parameters are independent of the salt concentration, and can be assessed from the specific experiments described in this paragraph.

A - Global Indirect Determination of $R_{i,m}$ by the Velocity Variation Method (VVM). The determination of the membrane-transport parameters (r_p, ε_p, X_d) requires the real rejection $R_{i,m}$. When the polarization layer cannot be neglected as considered in this article, $R_{i,m}$ calculation requires the concentration of the i-th specie at the wall ($C_{i,w}$), but this value cannot be obtained from standard experiments. In this study, an indirect method is used to estimate $R_{i,m}$, the velocity variation method (VVM).[50,51] The VVM relates the concentration of the i-specie in the bulk ($C_{i,r}$), and at the wall ($C_{i,w}$) through a mass-transfer coefficient between the membrane wall and the bulk solution k, in the framework of film theory (k being a *mean* coefficient over the membrane length).

The VVM consists, for a given permeation flux J_v, in determining the observed rejection $R_{i,obs}$ for various increasing tangential velocities, and in extrapolating these values to an infinite velocity $U_t = \infty$. The limit value such obtained is the real rejection $R_{i,m}$ that would correspond to a virtual situation where no polarization layer exists (that is, for which $C_{i,w}$ would be equal to $C_{i,r}$)

$$R_{i,m} = \lim_{U_t \to \infty} R_{obs}(U_t) \tag{39}$$

According to the film model, $R_{i,m}$ is related to the observed rejection through the following relation[14]

$$\ln\left(\frac{1 - R_{i,obs}}{R_{i,obs}}\right) = \ln\left(\frac{1 - R_{i,m}}{R_{i,m}}\right) + \frac{J_v}{k} \tag{40}$$

The mean mass-transfer coefficient k between the membrane wall and the bulk solution can be obtained from an empirical Sherwood relation ($Sh = a\mathrm{Re}^b\, Sc^c$), for instance, if the membrane is long enough to neglect the entrance effect. Introducing $Sh = \frac{kd_H}{D}$, $\mathrm{Re} = \frac{\rho U_t d_H}{\eta}$, and $Sc = \frac{\eta}{\rho D}$ into this equation leads to

$$k = KU_t{}^b \tag{41}$$

with $K = a\rho^{(b-c)}\, \eta^{(c-b)}\, D^{(1-c)}\, d_H{}^{(b-1)}$.

In this study, the Deissler equation was chosen for its range of validity (tubular module configuration, $\mathrm{Re} > 4{,}000$ and $1 \leq Sc \leq 1{,}000$[52]). In this equation, the values of the coefficients a, b and c are, respectively 0.023, 0.875 and 0.25.[53]

Let us consider a set of experiments with a constant permeation flux J_v, and an increasing tangential velocity U_t. According to Eqs. 40 and 41, the coefficient K, and the limit real rejection $R_{i,m}$ can be determined graphically by plotting $\ln\left(\frac{1-R_{obs}}{R_{obs}}\right)$ as a function of $f\left(\frac{J_v}{U_t{}^b}\right)$. K is assessed from the slope of the curves and from the intercept ordinate. (see Figure 4).

The mass-transfer coefficient k estimated by the Deissler Eq. 41, and that estimated by the VVM from experimental results are in a good agreement (k varies from 6.5 to 10×10^{-5} m/s experimentally, and is 9.8×10^{-5} m/s with Deissler equation for $U_t = 1.9$ m/s). So the Deissler correlation seems to be suitable for a first estimation of the polarization effect. Figures 5a and 5b depict, respectively, the wall concentration $C_{i,w}$, and the observed rejection evolutions along the membrane obtained by the PPTM (profiles along the membrane and mean values), and the constant values given by the film model. These figures show that the film model can give a good approximation of the average wall concentration, and, thus, of the observed rejections, with few calculations. Nevertheless, by calculating a mean mass-transfer coefficient along the membrane, the concentration and rejection profiles (in the polarization layer) cannot be predicted. Only a 2-D model can represent correctly the axial heterogeneity of mass transfer along the membrane. With a 2-D model, the concentration gradient along the membrane is predicted. It shows that the values of both rejections and permeation fluxes clearly vary between the inlet and the outlet of the membrane. Moreover, these variations could be much more significant in the case of small filtration module for which entrance effects are more important.

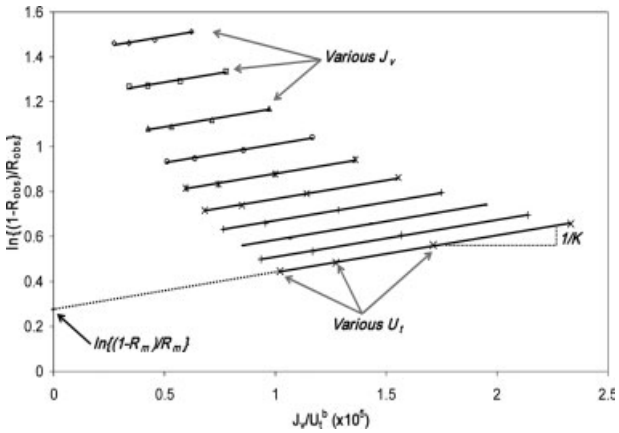

Figure 4. Example of the determination of mass-transfer coefficient k, and real rejection $R_{i,m}$, with the velocity variation method (for a 0.2 M NaCl solution).

Thereafter, the VVM is used only to estimate the membrane parameters when the polarization layer cannot be neglected. Indeed, for simulation runs, the VVM is not used and the polarization layer is described by a turbulent transport in the hydrodynamic sublayers.

B - Membrane Permeability and Average Pore Radius. Membrane permeability L_p is determined before each experiment by measuring the pure water permeation flux J_w, for various transmembrane pressures ΔP. Permeability of the AFC40 membrane was found to remain nearly constant for each set of experiments (NaCl or $MgCl_2$), with values $L_p = (1{,}30 \pm 0{,}05) \times 10^{-14}$ m for NaCl experiments, and $L_p = (1{,}61 \pm 0{,}02) \times 10^{-14}$ m. The values are different because a chemical cleaning was carried out between these two set of experiments.

The average pore radius r_p, of the active layer is assessed through an indirect method from experimental measures for which rejection is only governed by steric effects. In this

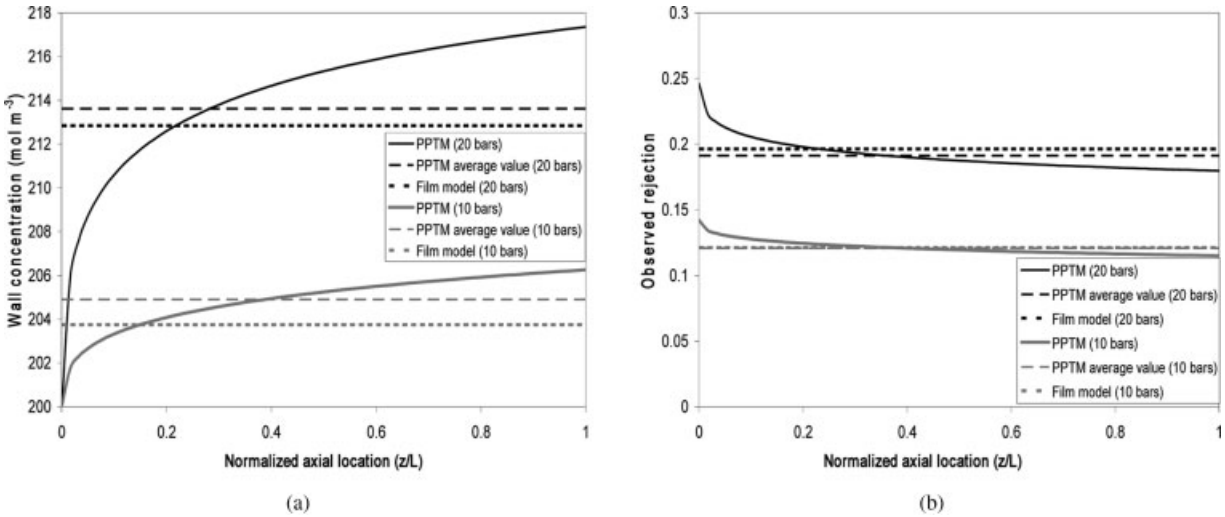

Figure 5. Wall concentration (a), and observed rejection (b) evolutions along the membrane for two applied pressures estimated by 2-D simulations, and by the film model (0.2 M NaCl solution).

study, r_p were estimated by fitting real rejections, determined by the variation velocity method, with the following equation [54]

$$R_{i,m} = 1 - \frac{\phi K_c}{1 - (1 - \phi K_c)\exp\left(-\frac{K_c {r_p}^2 \Delta P_e}{8\eta K_d D_\infty}\right)} \tag{42}$$

The average pore radius r_p was estimated by fitting rejection curves obtained with a 0.02M glucose solution (Figure 6), with Eq. 42, and the estimated value that will be employed, hereafter, in the model is 0.53 nm. This value is in good agreement with the results obtained by Szymczyk et al.,[29] who find an average pore diameter for an AFC30 membrane of 0.50 nm. Our value is rather higher, which is coherent with the fact that rejections of AFC40 membranes are lower than that of AFC30 membranes.

Knowing the value of pore radius r_p, the effective thickness of the membrane $\Delta x/A_k$ can be estimated because the velocity in the pores can be written as in Eq. 4 with $\Delta\pi = 0$,

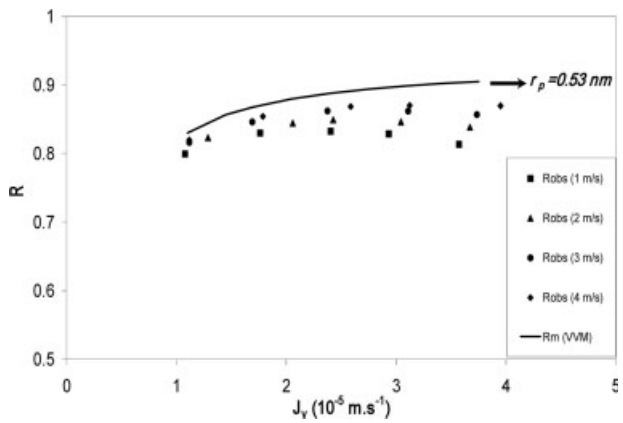

Figure 6. Observed and real rejections of a 0.02 M glucose solution at various velocities.

or as $V = \frac{J_v}{A_k} = \frac{L_p \Delta P}{\eta A_k}$, with A_k the membrane porosity. This leads to $\frac{\Delta x}{A_k} = \frac{{r_p}^2}{8L_p} = 21.6\mu$m for NaCl experiments (before chemical cleaning), and 17.5 μm for $MgCl_2$ experiments (after chemical cleaning).

C - Dielectric Constant of Solvent in the Pore. Dielectric effects are often taken into account by considering that the dielectric constant of the solvent within the pore ε_p, differs from that in the bulk solution. This decrease of the dielectric constant within the pores is usually attributed to confinement, but recent works[55,56] devoted to the study of this dielectric constant have shown that this decrease could be probably also attributed to external electric field induced by membrane fixed charges. This electrical field is expected to order solvent molecules dipoles, and, thus, to decrease the dielectric constant of the solvent. Nevertheless, the value of ε_p is kept constant in this work whatever the concentrations. This assumption is reasonable as experiments are performed at a constant pH value, and, thus, a constant membrane fixed charge. The value of ε_p is determined by considering the Born effect through experiments where electric effects (Donnan) can be neglected, allowing investigation of steric and dielectric effects only. Bowen et al.[38] have proposed to fit experimental rejection of salts at the membrane isoelectric point for which the membrane is uncharged. In our case, it was not possible because pH has a very great influence on pore diameter, as well as on rejection (up to 100 %), as it is shown on Figure 7, which depicts the influence of acid and basic cleaning on NaCl, and glucose rejections for the same range of pressure. On this graph, important variations of flux and rejection are observed consecutively to membrane cleanings. These variations can be explained by the increases of the membrane water permeability (1.894 to 3.15 10^{-14} $m^3 m^{-2} s^{-1}$), and pore radius (0.43 to 0.56 nm).

In this work, ε_p is assessed by fitting the real rejection curve obtained by VVM for quite concentrated salt solutions, for which it is assumed that membrane charges are totally screened by solution charges ($X_d/C_{i,w} \rightarrow 0$). Figure 8 clearly shows that for a concentration higher than 0.4 M, the rejec-

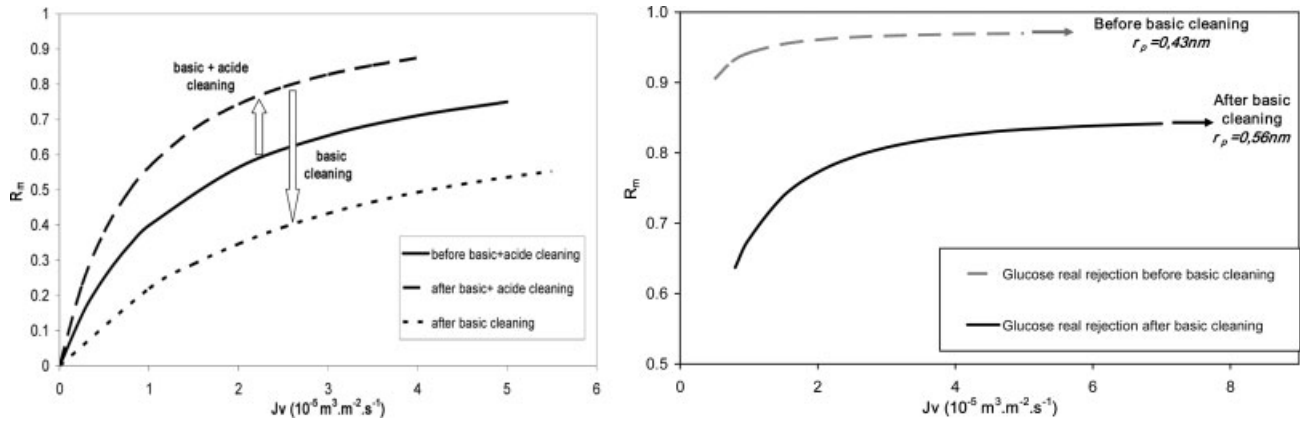

Figure 7. Influence of basic and acid cleanings on glucose and NaCl real rejections.

tion of NaCl remains constant, which seems to confirm the assumption that membrane charge density can be neglected at this concentration. This figure also shows that for magnesium chloride solutions membrane charges appear to be screened for a lower concentration (0.1 M), probably due to the magnesium ion. Indeed, the screening effect was found to be more relevant for divalent cations as it was described by Morao et al.[57] For this reason, a 0.4 M NaCl and 0.2 M KCl concentrations were chosen in this work. Fitting real rejection at these concentrations with a membrane charge density equals to zero gives 59.3 for NaCl, and 61.2 for $MgCl_2$. The obtained values are realistic and close to those estimated with KCl solutions by Szymckzyk et al.[29] for AFC membrane (ranging from 42 to 59 depending on the electrolyte and its concentration), which are coherent with the values (from 42 to 55) estimated by Senapati and Chandra[58] with molecular dynamics simulations for water confined in a nanodimensional spherical cavity.

The dielectric constant of the solution within the pores ε_p has been reassessed by including also the "image forces" effect, both Born and "image forces" effects being coded into the model. Rejections for concentrated solutions (NaCl 0.4 M and $MgCl_2$ 0.2 M) were used as previously described to estimate ε_p, no new adjustable parameter is being required to model the "image forces". With these solutions, it was found that no realistic values of ε_p allow a good prediction of experimental salt rejections. Indeed, the ε_p-values obtained in this way for concentrated solutions were greater than that of the bulk solution (ε_b = 78.4), which is inconsistent with its physical meaning. A similar result was previously observed by Szymczyk et al. for filtration of $CaCl_2$ solutions on the same membrane used in this work operating in the lower limiting case (X_d = 0). Thus, even by considering only the "image forces" effect (that is, by taking $\varepsilon_p = \varepsilon_b$), the experimental rejections cannot be fitted correctly (see Figure 9). These results have nevertheless to be interpreted carefully, because incoherencies can result from the indirect determination of ε_p at high-salt concentration. Low-rejections obtained in this work at highly concentrated solutions seem to be unpredictable by both "image forces" and Born effects except by increasing the dielectric constant of the membrane material (for example, ε_m=10 for NaCl, and 17 for $MgCl_2$ instead of 3). So, only the Born effect was considered in this work.

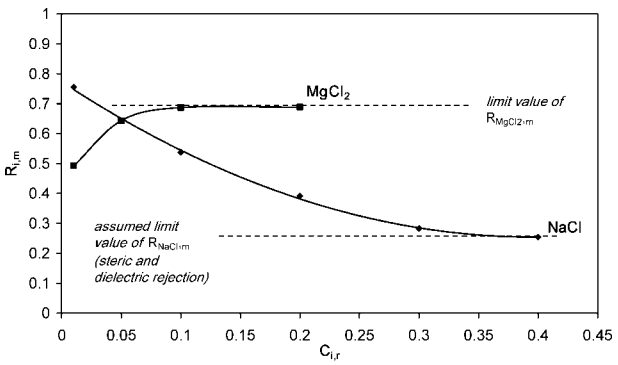

Figure 8. Real rejection evolution with feed concentration for NaCl and $MgCl_2$.

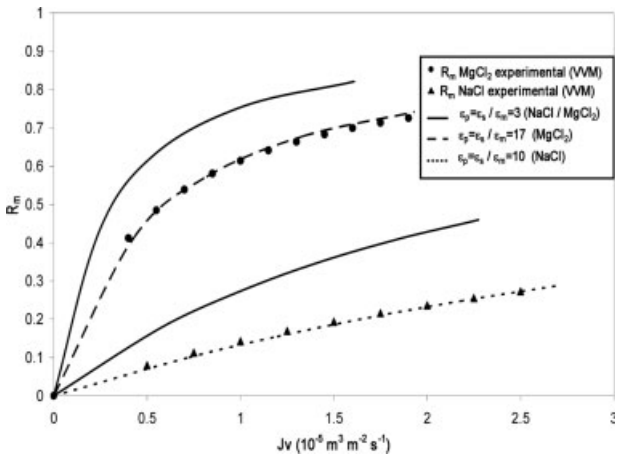

Figure 9. Real rejections of concentrated solutions, obtained by VVM (•), and simulated (—) with only the "image forces" dielectric effect (with $\varepsilon_p = \varepsilon_b$ = 78.4, and by adjusting the dielectric constant of the membrane material ε_m).

Table 2. Effective Membrane Charge Densities Obtained by the 1-D Membrane Model with Bulk Feed Concentration

Wall Salt Concentration $C_{i,w}$ (mol m^{-3})	Effective Charge Density X_d (mol m^{-3}) for Solutions of		Ratio $\|X_d\|/C_{i,w}$	
	NaCl	$MgCl_2$	NaCl	$MgCl_2$
10	−30	−1.7	3	0.17
50	−87	−1.2	1.75	0.024
100	−130	0	1.3	0
200	−135	–	0.68	–
300	−90	–	0.3	–

D - Membrane charge density

Membrane charge density is estimated by fitting the real rejection curves obtained from experimental data by the velocity variation method. In such a way, a membrane charge density X_d is assessed for a given bulk concentration, which is supposed to be the wall concentration $C_{i,w}$. The X_d value obtained through the VVM is considered by some authors as function of $C_{i,w}$ according to a Langmuir-type[59] or Freundlich-type[60,61] isotherm adsorption. However, other authors[7] consider that correlating X_d to the ions mole fractions in the pore is more physically coherent. In this study, it was assumed that charge formation mechanisms occur mainly at the interface between the membrane and the feed solution which appears to be consistent with the small pore size. For this reason, the membrane charge density was correlated to the wall concentration $C_{i,w}$.

At moderate concentration ($C_{i,r} \leq$ 0.1M), membrane charge densities obtained in this way are physically coherent with an adsorption-like law, that is, X_d increases with $C_{i,w}$ with a negative curvature. In addition, for NaCl solutions, it can be seen in Table 2 that the ratio of effective charge density to wall concentration $|X_d|/C_{i,w}$ decreases and tends toward zero when $C_{i,w}$ increases, which results from membrane charges screening by solution charges. For NaCl concentrations higher than 0.1 M, the identified membrane charge density does not increase anymore and even decreases for high-concentration. A similar behavior (that is, an increase and then a decrease of X_d when concentration increases) was reported by Mazzoni et al.[62] from experiments carried out with $CaCl_2$ solutions.

Figure 10 gives a graphical representation of real rejections of NaCl and $MgCl_2$, $R_{i,m}$ obtained experimentally by the VVM and simulated with the 1-D model for various membrane charge densities X_d. This figure shows a really good agreement between experimental rejections, and simulated ones obtained with given membrane charge densities for both NaCl and $MgCl_2$.

It is worth remarking that NaCl and $MgCl_2$ rejection evolution when the salt concentration $C_{i,r}$ increases are opposite. Indeed, NaCl rejection decreases as $C_{i,r}$ increases, whereas $MgCl_2$ rejection increases. A similar observation has been reported by Bandini and Vezzani[39] for another nonsymmetric salt with a divalent cation $CaCl_2$. This fact can be explained by the Donnan electrostatic exclusion phenomenon. Indeed, a negatively charged membrane tends to attract (positive) counterion, and to repel (negative) coion. When the salt concentration increases, the ratio $|X_d|/C_{i,w}$ decreases, and, therefore, the counterions are less attracted, and the coions are less repelled. It can be assumed that for a nonsymmetric salt with a divalent counterion, the first effect (counterion less attracted) is quantitatively predominant compared with the second one (coion less repelled).

This can also explain that the membrane charge density X_d identified through the model decreases as the salt concentration $C_{i,r}$ increases for $MgCl_2$, but increases for NaCl.

Finally, it can also be remarked that membrane charge densities obtained for $MgCl_2$ solutions are clearly lower than those obtained for NaCl solutions (−1.2 to −1.7 mol m^{-3} for $MgCl_2$ concentration from 10 to 50 mol m^{-3}, −30 to −135 mol m^{-3} for NaCl concentration from 10 to 200 mol m^{-3}). The decrease in X_d between NaCl and $MgCl_2$ solutions is consistent with the fact that the negative membrane surface charge is more shielded by the excess of

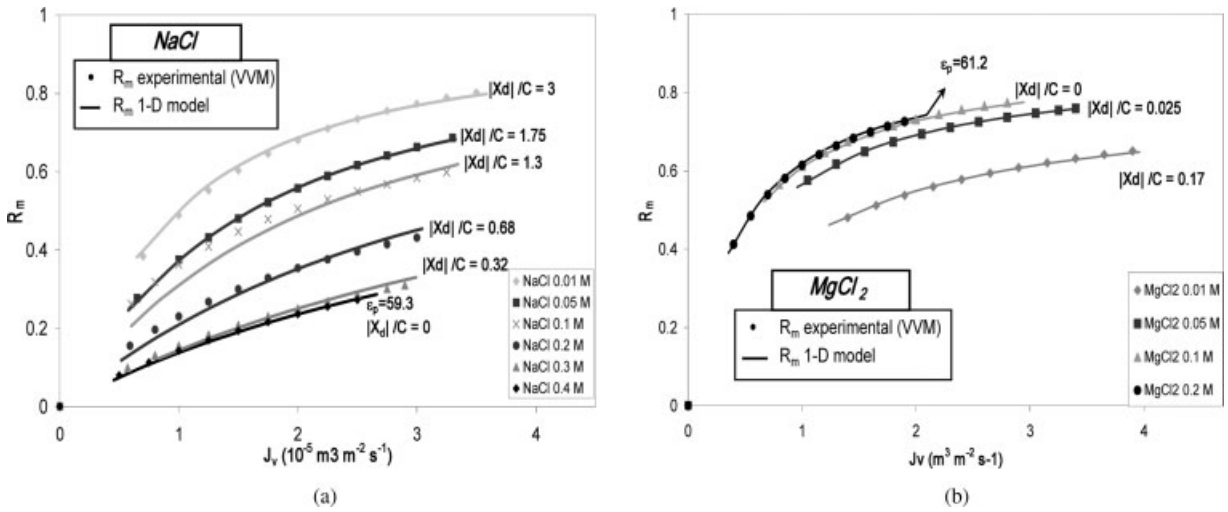

Figure 10. Real rejections evolution with permeation flux for various bulk concentrations of NaCl (a), and $MgCl_2$ (b), obtained by VVM (•) and by 1-D simulations with adjusted X_d-values (—).

divalent cations in the surface vicinity than by that of monovalent cations, as previously reported by Morao et al.[57] and Bandini et al.[39] Nevertheless, X_d values seem to be very low for $MgCl_2$ comparatively to those obtained for NaCl.

However, the low X_d values can also be explained by the fact that the Mg^{2+} adsorption has a greater impact on the effective membrane charge density. Mazzoni et al.[62] have also obtained very low-membrane charge densities for $CaCl_2$ solutions with a concentration of up to 0.05 M. They also observed a switch of the charge density to positive values. Their results could be explained either by a greater impact of Ca^{2+} on charge density (which could switch the effective charge to positive values), or by the fact that dielectric constant within the pores is supposed to be that of the solution in their model. In addition, obtained values of X_d must be considered with caution, in as much as both X_d and ε_p values have been determined indirectly, namely by identification through the model. Now, an infinite number of couple (X_d, ε_p) can explain a given set of experimental rejections, because electrostatic and dielectric exclusion both contribute to reject ions outside the membrane. For instance, an increase in ε_p (decrease in dielectric exclusion) can be balanced by an increase in X_d (increase in electrostatic exclusion). In addition, a sensibility analysis has shown that a small variation in ε_p leads to a great change in X_d.

For moderate NaCl concentration (up to 0.1 M), identified X_d values increases with $C_{i,w}$. Figure 11 shows that X_d can be correlated on this range to $C_{i,w}$ either through a Freundlich isotherm (Eq. 43a), or a Langmuir isotherm (Eq. 43b)

$$|X_d| = 7.57 C_{NaCl,w}^{0.62} \tag{43a}$$

$$|X_d| = \frac{2.81 C_{NaCl,w}}{1 + 1.18\ 10^{-2} C_{NaCl,w}} \tag{43b}$$

At the opposite, it has been seen that for high NaCl concentrations (0.2 to 0.4 M), identified X_d-values decreases when $C_{i,w}$ increases, as observed for $MgCl_2$ at any concentration. This behavior could be attributed also to the screening of the negative membrane surface charge by the excess of Na^+ counterion in the vicinity of the surface.

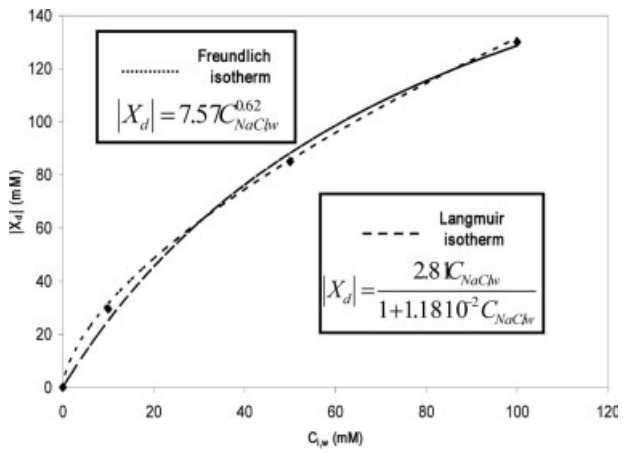

Figure 11. NaCl adsorption isotherms (X_d evolution with NaCl concentration) (0.01 to 0.1 M).

To conclude, it should be noted that membrane charges density can be clearly affected by a chemical cleaning, making quite tedious the comparison with results reported in the literature. Thus, we observed that the NaCl rejection was divided by about two after a standard chemical cleaning has been done (−135 to −67 for 0.2 M NaCl).

2-D Polarization model adjustment

Sensitivity study of the various model parameters has shown that good prediction of the experimental observed rejections evolution (with permeation flux) can be obtained only by increasing the salt molecular diffusivity at the membrane interface appearing in the boundary (Eq. 21). The increase of diffusion at the membrane interface could be explained by several physical phenomena, such as the presence of suction through pores or roughness at the membrane surface, which could cause weak flow perturbations very close to the wall. Indeed, computed fluid mechanics (CFM) simulations with Fluent have shown that the presence of pores and permeation can induce changes in velocity vectors directions near the wall. This backmixing could lead to an effective diffusivity at the wall significantly higher than the bulk diffusivity. This backmixing likely depends on the tangential velocity U_t, and the permeation flux J_v. In order to simplify the estimation of the "wall diffusivity", it was chosen nevertheless to correlate it with the tangential velocity only. The so-called "wall salt diffusivity" is then defined as

$$D_{s,w} = \alpha(U_t) D_{s,m} \tag{44}$$

where $\alpha(U_t)$ is the factor representing the increase of the salt diffusivity with the tangential velocity U_t. This α coefficient, is, thus, the adjustable parameter of the polarization modeling, and its evolution with velocity is required for predictive purposes.

The 2-D global model is then used to determine α values for each velocity. The values, given in Table 3, appear to increase quite linearly with tangential velocity which is coherent with the idea that this increase is due to weak perturbations very closed to the wall. These values, obtained with a 0.4 M NaCl solution will be validated afterward by experiments carried out with more diluted solutions.

Simulations with the 2-D PPTM

In this paragraph, the influence of the various experimental parameters on the polarization layer is first described before comparing some experimental results with 2-D model predictions. In this part, the PPTM and especially the polarization modeling are validated.

A - Influence of Hydrodynamic Conditions on Polarization Layer. In this paragraph, the influence of hydrodynamic parameters, tangential velocity U_t and transmembrane pressure ΔP, on ions accumulation at the membrane surface and on ions rejection is discussed. The results presented here are related to a 0.2 M NaCl. It is checked here whether simulated results are coherent with the physical knowledge about the polarization layer behavior. The setting-up of the concentration polarization layer is described through a salt mass bal-

Table 3. Evolution of the So-called "wall diffusion" with Tangential Velocity for 0.2 M NaCl Solution

Tangential Velocity U_t (m/s)	Factor of Wall Influence on "wall diffusion" α	The So-called "wall diffusion" $D_{i,w}$ (10^{-9} m^2/s)
1.32	2.3	3.69
1.89	2.6	4.18
2.73	3.1	4.98
3.5	3.5	5.62

ance integrated along the whole module (see the Physical description section).

Figure 12 presents simulated values of the wall concentration profile along the membrane $C_{i,w}(z)$, for different velocities and permeation flux. It can be seen in this figure that, even for low-velocities, the membrane is not long enough to obtain the whole polarization layer establishment. In addition, entrance effects appears to be non negligible, and could turn out to be significant for short membranes. These observations prove the interest to take account of the concentration evolution along the membrane with a 2-D model of polarization layer.

Figure 13a shows the evolution of observed rejection $R_{i,obs}$ along the membrane for $\Delta P = 20$ bar, and various tangential velocities U_t, as well as the real rejection $R_{i,m}$. It could be noted from this figure that $R_{i,obs}$ decreases along the membrane for a given tangential velocities, and that it increases with the tangential velocity because of the diminution of the polarization layer thickness. On the other hand, the real rejection $R_{i,m}$ remains quite constant because charges effects are negligible at this relatively high-salt concentration, and $R_{i,m}$ is independent of the hydrodynamic conditions and solute accumulation. In fact, J_v varies with U_t, and along the membrane, but changes in J_v remain very small (Figure 13b), because the osmotic pressure variation for NaCl is rather low. So, the impact of J_v on $R_{i,m}$ in Figure 13a cannot be distinguished.

Figure 14 depicts the radial NaCl concentration profile in the polarization layer at the middle of the membrane for various tangential velocities (Figure 14a), or various transmembrane pressures (Figure 14b). From this figure, it can be concluded that circulation velocity and permeation flux have a different influence on polarization layer. Velocity does not act much on the shape of the concentration profile, but it mainly reduces the thickness of the hydrodynamic layers, and, thus, that of the concentration polarization layer. In the opposite, permeation flux (pressure difference across the membrane) does not influence the layer thickness, but affects strongly the salt concentration gradient.

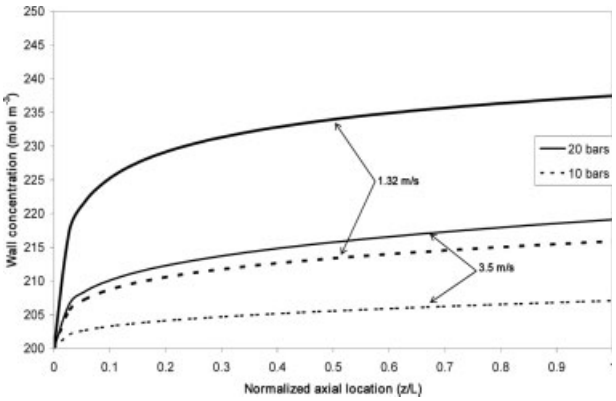

Figure 12. Wall concentration evolution along the membrane for various tangential velocities and applied pressure differences (obtained by 2-D simulations with 0.2 M NaCl solution).

Many authors assume that the mass boundary layer is wholly contained in the hydrodynamic laminar layer.[63] However, Figure 14 proves that polarization layer thickness reaches the buffer layer, especially for high-tangential velocities and high applied pressure differences. This conclusion justifies our approach which includes the three hydrodynamic sublayers.

B - Comparison between Experimental and Simulated Results. The last step for validating the polarization model consists in comparing experimental and simulated rejections

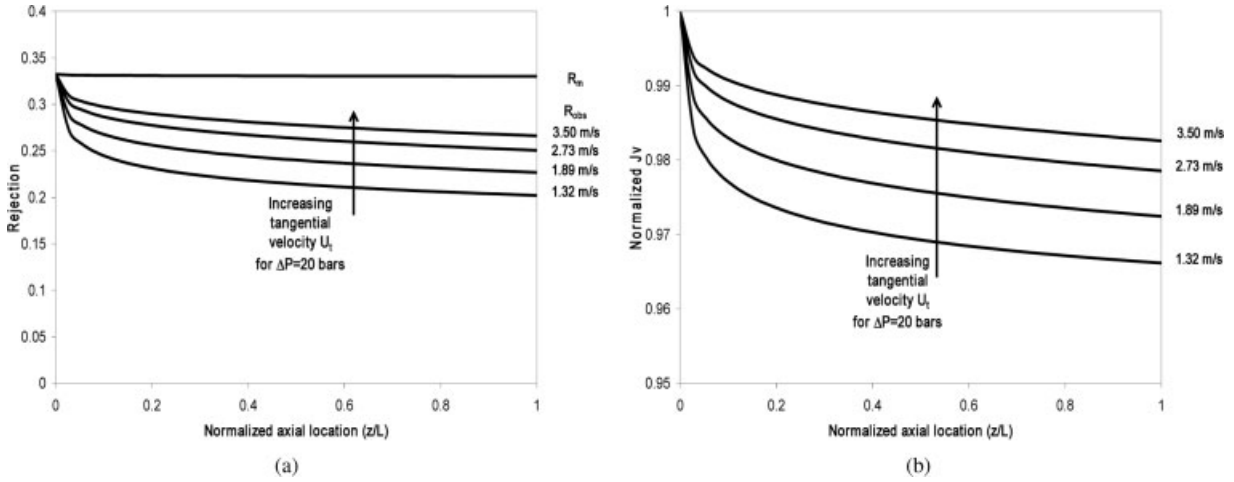

Figure 13. Evolution of observed and real rejections (a), and permeation flux (b) along the membrane for various velocities (obtained by 2-D simulations with 0.2 M NaCl solution).

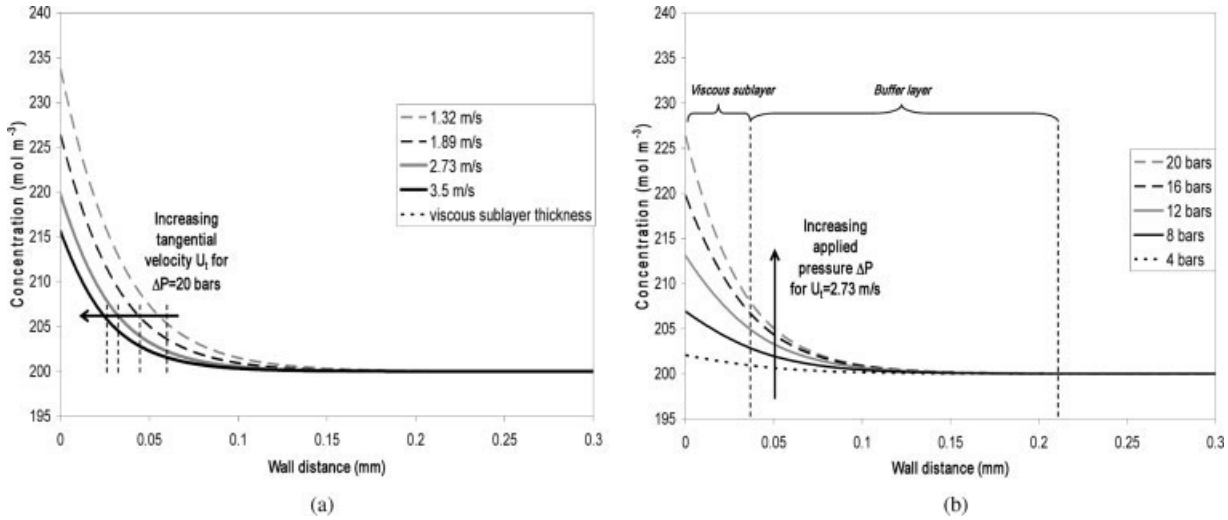

Figure 14. Concentration evolution within the polarization layer for various tangential velocities (a), and applied pressure differences (b) (obtained by 2-D simulations at the middle of the membrane with 0.2 M NaCl solution).

in cases where charge effects cannot be neglected. Therefore, the law $|X_d| = f(C_{i,w})$ is introduced into the 2-D model, and the charge density is assessed for each $C_{i,w}$ calculated by the model. The values of the diffusivity factor α are estimated by a linear law obtained with various NaCl concentrations, so that there is no adjustable parameter.

Figure 15 gives a graphical representation of the observed and real rejections ($R_{i,obs}$, $R_{i,m}$) simulated by the 2-D model, and obtained experimentally for two solutions (0.01 M NaCl and 0.01 M $MgCl_2$). This figure illustrates the fact that the polarization model predicts correctly the influence of hydrodynamic parameters, that is, observed rejection increases with transmembrane pressure at constant tangential velocity, and with tangential velocity at constant pressure. In this figure, it appears that the 2-D PPTM can predict the real rejection, via the adsorption-like law obtained previously and observed rejections are also really well-predicted via the linear law between the α coefficient and the tangential velocity for monavalent salt (NaCl), as well as divalent salts ($MgCl_2$). These observations seem to validate the assumption that the $\alpha-$factor representing the diffusivity increase at the membrane wall can be correlated with respect to tangential velocity only. Indeed, α was found to be independent of permeation and salt nature, as well as salt concentration as shown in Figure 16. This figure depicts the evolution of experimental and simulated (obtained with the α-law) observed rejections for various feed concentrations $C_{i,r}$, and tangential velocities at the same reference pressure (18 bars). The good agreement between the real rejections estimated by the velocity variation method, and the simulations tends to show that physical phenomena occurring within the membrane during salt rejection are well-described by the model.

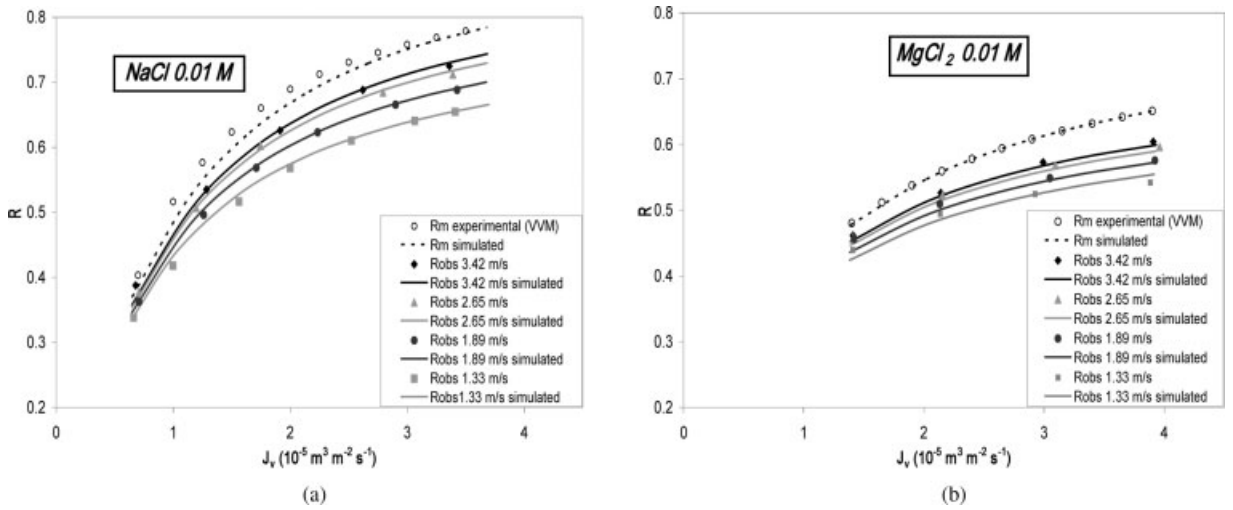

Figure 15. Real and observed rejections evolution with permeation flux for various velocities, obtained by experiments (•), and simulations (—) ((a) 0.01 M NaCl, and (b) 0.01 M $MgCl_2$ solutions).

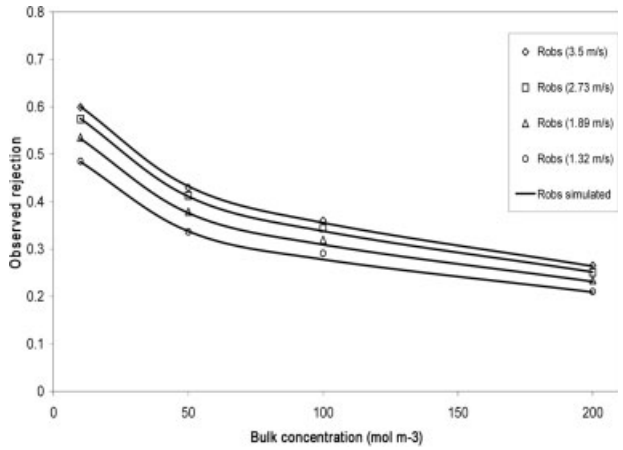

Figure 16. Evolution of observed rejections with NaCl bulk concentration for various velocities, obtained by experiments (•), and 2-D simulations (—) {ΔP=18 bars}.

Conclusion

A model for the transport of ionic solutions through an organic nanofiltration membrane called "Pore and Polarization Transport Model" (PPTM) was presented. This model includes the various phenomena usually referenced in the literature, such as interface steric, electric and dielectric exclusion effects, the various driving forces acting on ionic fluxes through the membrane pores according to the Nernst-Planck approach, and solutes transport in the concentration polarization layer. Polarization layer is usually neglected in the literature or limited to the viscous hydrodynamic sublayer. In this article, it was supposed that the concentration polarization layer is spread out not only within the laminar sublayer, but also within the buffer layer where eddy transport must be considered. Eddy transport has been described here using the eddy diffusivity and Prandtl mixing length concepts. This model has been applied to concentrated and diluted single salt solutions (NaCl and $MgCl_2$).

It has been also shown that the diffusion coefficient at the membrane interface has to be reassessed to depict correctly hydrodynamic effects at the membrane wall. Indeed, membrane wall roughness and maybe suction increase backmixing very close to the wall, and, consequently, solute diffusion. A "wall diffusivity factor" α has been introduced to represent these effects. This α factor was supposed to depend on tangential velocity only, and was determined from experiments on a quite concentrated NaCl solution for which membrane charge effects have been neglected. Values of α increase straightforwardly with the tangential velocity U_t, which consolidates the physical meaning of this parameter.

The estimated values of the model parameters could probably be improved by taking account of other complex phenomena, such as the influence of the so-called "image forces" on the equilibrium partitioning or the electroviscous effects on the permeation flux. Nevertheless, values of the model parameters occurring for the transfer through the membrane (r_p, ε_p, X_d), as well as their evolution with experimental conditions was found to be in good agreement with those presented in the literature.

Moreover, the 2-D model was validated with NaCl and $MgCl_2$ solutions by simulating evolution of real and observed rejections with applied pressure and tangential velocity via the adsorption law and the α evolution law defined with other experiments. These predictive simulations, carried out for NaCl and $MgCl_2$, gives results in a very good agreement with the experimental ones proving that the 2-D PPTM presented here is validated.

The developed model, can, thus, be used to predict accurately rejections, flux and the various profiles along the membrane for single salt (monavalent or divalent) solutions for various hydrodynamic conditions (salt concentration, applied pressure, and tangential velocity).

The model will be also tested later on with other single salts and salt mixtures, as well as with mineral ultrafiltration membranes with a low-molecular-weight cut-off.

Acknowledgments

The authors thank the French Ministry of Research & Technology for their financial support.

Notation

a = parameter
a_i = activity of ion i, mol m^{-3}
A_k = membrane porosity, dimensionless
c_i = concentration of ion i within the pore, mol m^{-3}
C_i = concentration of ion i within the polarization layer, mol m^{-3}
$C_{i,p}$ = permeate concentration of ion i, mol m^{-3}
$C_{i,r}$ = bulk concentration of ion i, mol m^{-3}
$C_{i,w}$ = wall concentration of ion i, mol m^{-3}
$D_{i,\infty}$ = molecular-diffusion coefficient of ion i at infinite dilution, m^2 s^{-1}
$D_{i,m}$ = molecular-diffusion coefficient of ion i, m^2 s^{-1}
$D_{i,p}$ = pore-diffusion coefficient of ion i, m^2 s^{-1}
$D_{i,t}$ = turbulent-diffusion coefficient of ion i, m^2 s^{-1}
$D_{i,w}$ = diffusion coefficient of ion i at the wall, m^2 s^{-1}
e = electronic charge, 1.602177 10^{-19}C
F = Faraday constant, 96487 C mol^{-1}
G = coefficient in Eq. 18
I = ionic strength (mol m^{-3})
j_i = ionic flux of ion i, mol m^{-2} s^{-1})
J_v = volumetric-permeation flux (m^3 m^{-2} s^{-1})
J_w = water-permeation flux (m^3 m^{-2} s^{-1})
k = mass-transfer coefficient (m s^{-1})
k_B = Boltzmann constant, 1.38066 10^{-23} J K^{-1}
K = Karman constant (dimensionless), Eq. 28a, or constant in Eq. 41
$K_{i,c}$ = ionic hindrance factor for convection, dimensionless
$K_{i,d}$ = ionic hindrance factor for diffusion, dimensionless
l = Prandtl's mixing length, m
L_p = water permeability, m^3 m^{-2}
P = pressure, Pa
R = universal gas constant, 8.314 J mol^{-1} K^{-1}
r_i = Stokes radius of ion i, m
$R_{i,m}$ = real rejection of ion i, dimensionless
$R_{i,m}^{\infty}$ = limit value of real rejection obtained by VVM, infinite tangential velocity
$R_{i,obs}$ = observed rejection of ion i, dimensionless
r_p = average pore radius, m
T = temperature, K
u = axial velocity within the flow, m s^{-1}
u^* = friction velocity, m s^{-1}
U_t = average tangential velocity, m s^{-1}
v = radial velocity within the flow, m s^{-1}
V = solvent velocity, m s^{-1}
$\bar{V}_i$ = partial molar volume of ion i, m^3 mol^{-1}
x = axial position within the pore, m

X_d = membrane effective charge density, mol m^{-3}
y = radial wall distance, m
y_+ = normalized wall distance, dimensionless
z = axial position along the membrane, m
z_i = valence of ion i, dimensionless

Greek letters

α = factor manifesting diffusion increase at the wall, dimensionless
β = Bjerrum radius, m
$\Delta\Pi$ = applied pressure, Pa
$\Delta W_{i,born}$ = born solvation energy barrier, J
Δx = membrane thickness, m
$\Delta\psi_D$ = Donnan potential, V
$\Delta\pi$ = osmotic pressure difference, Pa
ϕ_i = steric-partition coefficient, dimensionless
ϕ_i' = partition coefficient including activity coefficient, steric and dielectric effects
ψ = electrical potential within the pore, V
δ = polarization layer thickness, m
ε_0 = permittivity of free space, 8.85419 10^{-19} C
ε_b = bulk dielectric constant, dimensionless
ε_p = pore dielectric constant, dimensionless
$\gamma_{i,m}$ = activity coefficient of ion i in the pore side of the interface, dimensionless
$\gamma_{i,s}$ = activity coefficient of ion i in the solution side of the interface, dimensionless
η = dynamic viscosity within pores, Pa s
η_0 = bulk viscosity, Pa s
ν = kinematic viscosity, m^2 s^{-1}
ν_t = turbulent kinematic viscosity, m^2 s^{-1}
λ_i = ratio of ion stokes radius to pore radius, dimensionless

Literature Cited

1. Combe C, Guizard C, Aimar P, Sanchez V. Experimental determination of four characteristics used to predict the retention of a ceramic nanofiltration membrane. *J Membr Sci*. 1997;129:147–160.
2. Gross RJ, Osterle JF. Membrane transport caracteristics of ultrafine capillaries. *J Chem Phys*. 1968;49:228–234.
3. Dresner L. Some remarks on the integration of extended Nernst-Planck equation in the hyperfiltration of multicomponent solutions. *Desalination*. 1972;10:27–46.
4. Hunter RJ. Zeta potential in colloid science. Principles and applications. 1981.
5. Schlögl R. Membrane permeation in system far from equilibrium. *Berichte der Bunsengesellschaft Physik. Chem*. 1966;70:400.
6. Noordman TR, Wesselingh JA. Transport of large molecules through membranes wiyh narrow pores. The Maxwell-Stefan description combined with hydrodynamic theory. *J Membr Sci*. 2002;210:227.
7. Straatsma J, Bargeman G, van der Horst HC, Wesselingh JA. Can nanofiltration be fully predicted by a model? *J Membr Sci*. 2002;198:273–284.
8. Krishna R, Wesselingh JA. The Maxwell-Stefan approach to mass transfert. *Chem Eng Sci*. 1997;52:861–911.
9. Kedem O, Katchalsky A. Permeability of composite membranes. *Trans Faraday Soc*. 1963;59:1941–1953.
10. Spiegler KS, Kedem O. Thermodynamics of hyperfiltration (Reverse Osmosis): criteria for coefficient membranes. *Desalination*. 1966; 1:311–326.
11. Murthy ZVP, Gupta SK. Estimation of mass transfer coefficient using a combined nonlinear membrane transport and film theory model. *Desalination*. 1997;109:39–49.
12. Zydney AL. Stagnant film model for concentration polarization in membrane systems. *J Membr Sci*. 1997;130:275–281.
13. Lefebvre X. Etude des modèles de transfert en nanofiltration. Application du modèle hybride basé sur les équations de Nernst-Planck étendues par le développement du logiciel de simulation "Nanoflux". Université de Montpellier II, Montpellier; 2003. PhD Theses.
14. Van den Berg GB, Racz IG, Smolders CA. Mass transfer coefficients in cross-flow ultrafiltration. *J Membr Sci*. 1989;47:25–51.
15. Bhattacharjee S, Chen JC, Elimelech M. Coupled model of concentration polarization and pore transport in cross flow nanofiltration. *AIChE J*. 2001;47:2733–2745.
16. Bowen WR, Mohammad AW. Diafiltration by nanofiltration: prediction and optimization. *AIChE J*. 1998;44:1799–1812.
17. Anderson JL, Quinn JA. Restricted transport in small pores: a model for steric exclusion and hindered particle motion. *Biophys J*. 1974; 14:130–150.
18. Deen WM. Hindered transport of large molecules in liquid-filled pores. *AIChE J*. 1987;33:1409–1425.
19. Bowen WR, Mukhtar H. Characterisation and prediction of separation performance of nanofiltration membranes. *J of Membr Sci*. 1996;112:263–274.
20. Bowen WR, Cassey B, Jones P, Oatley DL. Modelling the performance of membrane nanofiltration-application to an industrially relevant separation. *J of Membr Sci*. 2004;242:211–220.
21. Hagmeyer G, Gimbel R. Modelling the rejection of nanofiltration membranes using zeta potential measurements. *Sep and Purification Technol*. 1999;15:19–30.
22. Schaep J, Vandecasteel C, Mohammad AW, Bowen WR. Analysis of salt retention of nanofiltration membranes using the Donnan-steric partioning pore model. *Sep Sci. Technol*. 1999;34(15):3009–3030.
23. Bowen WR, Welfoot JS, Williams PM. Linearized transport model for nanofiltration: development and assessment. *AIChE J*. 2002; 48:760–773.
24. Palmeri J, Sandeaux J, Sandeaux R, Lefebvre X, David P, Guizard C, Amblard P, Diaz J-F, Lamaze B. Modeling of multi-electrolyte transport in charged ceramic and organic nanofilters using the computer simulation program NanoFlux. *Desalination*. 2002;147:231–236.
25. Ferry JD. Statistical evaluation of sieve constants in ultrafiltration. *J Gen Physiol*. 1935;20:95–104.
26. Ferry JD. Ultrafilter membranes and ultrafiltration. *Chem Rev*. 1936; 18:373–455.
27. Deen WM, Satvat B, Jamieson M. Theoretical model for glomerular filtration of charged solutes. *Am J Physiol*. 1980;38:126–139.
28. Donnan FG. Theory of membrane equilibria and membrane potentials in the presence of non-dialysing electrolytes. A contribution to physical-chemical physiology. *J Membr Sci*. 1995;100:45–55.
29. Szymczyk A, Fievet P. Investigating transport properties of nanofiltration membranes by means of a steric, electric and dielectric exclusion model. *J Membr Sci*. 2005;252:77–88.
30. Hagmeyer G, Gimbel R. Modelling the salt rejection of nanofiltration membranes for ternary ion mixtures and for single salts at different pH values. *Desalination*. 1998;117:247–256.
31. Robinson RA, Stokes RH. *Electrolytes solutions*. Butterworths. 1965.
32. Newman J, Thomas-Alyea KE. *Electrochemical systems*. John Wiley & Sons, Inc.; 2004.
33. Dukhin SS, Churaev NV, Shilov VN, Starov VM. Problems in the modeling of reverse osmosis separation. *Russ Chem Rev*. 1988; 57:572–584.
34. Yaroshchuk AE. Dielectric exclusion of ions from membranes. *Ad Colloid Interf Sci*. 2000;85:193–230.
35. Yaroshchuk AE. Non-steric mechanisms of nanofiltration: superposition of Donnan and dielectric exclusion. *Sep Purif Technol*. 2001; 22–23:143–158.
36. Israelachvili JN. *Intermolecular and surface forces*. 2nd ed. London: Academic Press; 1991.
37. Born M. Volumen and hydratationswärme der ionen. *Z Physik Chem*. 1920;1:45.
38. Bowen WR, Welfoot JS. Modelling the performance of membrane nanofiltration-critical assessment and model development. *Chem Eng Sci*. 2002;57:1121–1137.
39. Bandini S, Vezzani D. Nanofiltration modeling: the role of dielectric exclusion in membrane characterization. *Chem Eng Sci*. 2003;58: 3303–3326.
40. Bhattacharjee S, Kim AS, Elimelech M. Concentration polarization of interacting solute particles in cross-flow membrane filtration. *J Colloid Interf Sci*. 1999;212:81–99.
41. Minnikanti VS, DasGupta S, De S. Prediction of mass transfer coefficient with suction for turbulent flow in cross flow ultrafiltration. *J Membr Sci*. 1999;157:227–239.
42. Paris J, Guichardon P, Charbit F. Transport phenomena in ultrafiltration: a new two-dimensional model compared with classical models. *J Membr Sci*. 2002;207:43–53.

43. Bird RB, Stewart WE, Lightfoot EN. *Transport phenomena*. John Wiley & Sons, Inc.; 2002.
44. Padet J. *Fluides en écoulements*. Paris: Masson. 1990.
45. Szymczyk A, Fievet P, Reggiani JC, Pagetti J. Characterisation of surface properties of ceramic membranes by streaming and membrane potentials. *J Membr Sci*. 1998;146:277–284.
46. Schaep J, Vandecasteele C. Evaluating the charge of nanofiltration membranes. *J Membr Sci*. 2001;188:129–136.
47. Fievet P, Szymczyk A, Aoubiza B, Pagetti J. Evaluation of three methods for the characterization of the membrane-solution interface: streaming potential, membrane potential and electrolyte conductivity inside pores. *J Membr Sci*. 2000;168:87–100.
48. Lide LR. *Handbook of chemistry and physics*. CRC Press; 1998.
49. Press WH, Flannery BP, Teukolsky SA, Vetterling WT. *Numerical recipes*. Cambridge University Press; 1986.
50. Jonsson G, Boesen CE. Concentration polarization in a reverse osmosis test cell. *Desalination*. 1977;21:1–10.
51. Nakao S, Kimura S. Analysis of solutes rejection in ultrafiltration. *J Chem Eng Jpn*. 1981;14:32–37.
52. Wijmans JG, Nakao S, Van Den Berg JWA, Troelstra FR, Smolders CA. Hydrodynamic resistance of concentration polarization boundary layers in ultrafiltration. *J Membr Sci*. 1985;22:117–135.
53. Gekas V, Hallstrom B. Mass transfer in the membrane concentration polarization layer under turbulent cross flow: I. Critical literature review and adaptation of existing sherwood correlations to membrane operations. *J Membr Sci*. 1987;30:153–170.
54. Combe C. Estimation de la sélectivité en nanofiltration à partir des propriétés du matériau membranaire. Modèles de transport. Université Paul Sabatier, Toulouse; 1996. PhD Theses.
55. Szymczyk A, Sbai M, Fievet P, Vidonne A. Transport properties and electrokinetic characterization of an amphoteric nanofilter. *Langmuir*. 2006;22:3910–3919.
56. Szymczyk A, Fievet P, Ramseyer C. Dielectric constant of electrolyte solutions confined in a charged nanofiltration membrane. *Desalination*. 2006;200:125–126.
57. Morao AIC, Alves AMB, Afonso MD. Concentration of clavulanic acid broths: Influence of the membrane surface charge density on NF operation. *J Membr Sci*. 2006;281:417–428.
58. Senapati S, Chandra A. Dielectric constant of water confined in a nanocavity. *J Phys Chem B*. 2001;105:5106–5109.
59. Bandini S. Modelling the mechanism of charge formation in NF membranes: Theory and application. *J Membr Sci*. 2005;264: 75–86.
60. Bowen WR, Mukhtar H. Characterisation and prediction of separation performance of nanofiltration membranes. *J Membr Sci*. 1996; 112:263–274.
61. Afonso MD. Surface charge on loose nanofiltration membranes. *Desalination International Congress on Membranes and Membrane Processes*. 2006;191:262–272.
62. Mazzoni C, Bandini S. On nanofiltration Desal-5 DK performances with calcium chloride-water solutions. *Sep Purif Technol*. 2006;52: 232–240.
63. De S, Bhattacharya PK. Mass transfer coefficient with suction including property variations in applications of cross-flow ultrafiltration. *Sep Purif Technol*. 1998;16:61–73.

Manuscript received July 6, 2006, revision received Feb. 21, 2007, and final revision received Apr. 11, 2007.